JOURNAL OF APPLIED CRYSTALLOGRAPHY
ISSN 1600-5767

Exact resolution function for double-disk chopper neutron time-of-flight spectrometers: application to reflectivity

Didier Lairez,[a,b]* Alexis Chennevière[a] and Frédéric Ott[a]

[a]Laboratoire Léon Brillouin, CEA–CNRS–Université Paris–Saclay, 91191 Gif-sur-Yvette, France, and [b]Laboratoire des solides irradiés, CEA–École polytechnique–CNRS–Institut Polytechnique de Paris, 91128 Palaiseau, France. *Correspondence e-mail: lairez@cea.fr

Received 15 October 2019
Accepted 7 February 2020

Edited by E. P. Gilbert, ANSTO, Kirrawee DC, Australia

Keywords: time-of-flight spectrometers; HERMÈS reflectometer; neutrons; resolution; reflectivity; exact resolution function; data fitting.

The exact resolution function of the transfer vector for the HERMÈS reflectometer at the Laboratoire Léon Brillouin is calculated as an example of a neutron time-of-flight spectrometer with a double-disk chopper. The calculation accounts for the wavelength distribution of the incident beam, the tilt of the chopper axis, collimation and gravity, without an assumption of Gaussian distributions or the independence of these different contributions. A numerical implementation is provided. It is shown that data fitting using this exact resolution function allows much better results to be reached than with the usual approximation by a Gaussian profile.

1. Introduction

It is quite common for physical measurements to attempt to reach the limit of a given technique. In many cases, this amounts to measuring a quantity with an accuracy better than the resolution of the apparatus. Stated like that, it seems impossible. For instance, how is one to discriminate the position of two peaks which are closer to each other than their width? It is possible to do this if we expect a given shape for each peak, by convoluting the expectation with the resolution function of the apparatus and comparing the result with the measurement (this is commonly called 'data fitting'). As another example, neutron specular reflectivity allows us to get structural information on thin layers at an interface, *i.e.* layer thicknesses and densities [for an introduction to reflectivity see, for instance, Cousin & Chennevière (2018)]. The latter are determined relative to the scattering length density difference $\Delta\rho$ between the two infinite media separated by the interface, and consequently from the value of the critical transfer vector q_c below which total reflection occurs; *e.g.* for the air/silicon interface $q_c = 0.0102$ Å^{-1} yields $\Delta\rho = q_c^2/16\pi = 2.07 \times 10^{10}$ cm^{-2}, which is the correct result. A shift of 3% for $q_c = 1.03 \times 0.0102$ Å^{-1} gives $\Delta\rho = 2.20 \times 10^{10}$ cm^{-2}, which is not acceptable for many users of reflectometers. But 3% is the order of magnitude of the resolution. This barrier can be bypassed if we know that the reflectivity curve should obey a given function. To reach these limits, the calculation of the resolution function has to be as accurate as possible. In particular, the approximation that all of the random variables that contribute to the resolution have a Gaussian probability density is probably not satisfactory (Nelson, 2013), especially in cases where the resolution is relaxed to gain flux. This approximation, which was legitimate when the means of calculation were insufficient, is no longer justified.

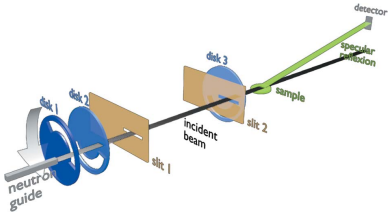

Neutron reflectivity measurements take a 'picture' of a sample in reciprocal space for which the conjugate variable of distance is the transfer vector **q**, whose magnitude is proportional to the ratio of the incident angle θ to the wavelength λ. Assuming that θ and λ are two independent variables, the relative resolution is such that $(\sigma_q/q)^2 \simeq (\sigma_\theta/\theta)^2 + (\sigma_\lambda/\lambda)^2$, where σ are the standard deviations. On the other hand, if we do not account for the transfer function of the sample, the signal is proportional to the incident neutron flux, *i.e.* to the product $\sigma_\theta\sigma_\lambda$. Thus for a given flux, the minimum in σ_q/q is obtained for $\sigma_\theta/\theta = \sigma_\lambda/\lambda$. Time-of-flight (t.o.f.) techniques do the work at constant θ (thus constant σ_θ/θ) as a function of λ. If we require a constant flux, since σ_θ/θ is constant, σ_λ/λ should also be constant. This is achieved with double-disk choppers (van Well, 1992) and this argument is the major reason why double-disk choppers are widely used. The counterpart is a broad-resolution σ_λ at long wavelength, precisely in the region where good accuracy is often needed (the edge of the total reflection plateau), hence the interest in making an exact calculation of the resolution function.

In this paper we present the calculation of the overall and exact resolution function for the HERMÈS reflectometer at the Laboratoire Léon Brillouin, the design of which is widely adopted at several neutron sources. In spite of its current continuous neutron source (the Orphée reactor), this spectrometer is based on the t.o.f. principle which will become generalized with the increase in the number of pulsed neutron sources, and it is equipped with a double-disk chopper that is now standard. The presented formalism to obtain the exact resolution function thus has a broad scope and could be easily transferred to other reflectometers or to other techniques such as small-angle scattering or diffraction.

For the most part, the different contributions to the final resolution have already been mentioned separately in the literature: the wavelength distribution of the incident beam, the tilt of the chopper axis, the beam size, collimation and gravity (van Well & Fredrikze, 2005; Nelson, 2013; Gutfreund *et al.*, 2018). However, considering all these different terms for the exact and 'all-in-one' resolution function requires special attention, because the different contributions are neither independent nor Gaussian, so they cannot simply be added and are quite intertwined. This is precisely the motivation of our paper. Here, the different random variables that contribute to the final resolution are presented in a uniform and comprehensive manner. The most important factor is that their variances are not just added by virtue of the central-limit theorem, as is usually done, but their exact distribution functions are considered and appropriately convoluted. We write analytically the whole resolution function that accounts for all terms without any assumption of Gaussian distributions or statistical independence. In addition, a Python module that implements these calculations numerically is provided (https://bitbucket.org/LLBhermes/pytof/). Finally, we show that data fitting using this exact resolution function allows us to reach much more accurate results than when using the usual approximation by a Gaussian profile.

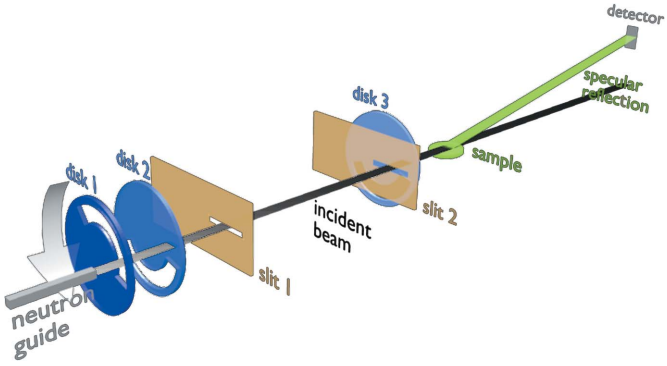

Figure 1
A schematic diagram of the HERMÈS reflectometer.

Table 1
Typical configurations corresponding to high, medium and low resolution.

x_1, x_2, x_3, x_s and x_d are the positions of disks 1, 2 and 3 and the sample and detector, respectively. r_1 and r_2 are the half-widths of the first and second slits of the collimator at a fixed distance d_c = 1800 mm apart. All lengths are in millimetres. Except where specified, the number of t.o.f. channels is equal to 256, covering 360° of chopper revolution. Also, the phases for disk 1 closure ($\varphi_{c,1}$) and disk 2 and disk 3 opening ($\varphi_{o,2}$, $\varphi_{o,3}$) are equal.

	HR	MR	LR
$x_d - x_s$		2020	
$x_d - x_3$		2375	
$x_3 - x_2$		2000	
$x_2 - x_1$	100	350	1000
r_1	0.5	1	2.3
r_2	0.5	0.5	0.5

2. Brief description of the reflectometer

In Fig. 1, a schematic diagram of the HERMÈS reflectometer is shown. Neutron pulses are produced by a three-disk chopper from Airbus. The three disks (numbered 1, 2 and 3 with respect to the neutron direction) have the same radius r = 300 mm and the same fixed angular aperture of 165° allowing neutrons to pass. In standard configurations these disks rotate in the same direction at a pulsation ω around the same axis. Disks 2 and 3 are in fixed positions 2 m from each other, whereas disk 1 can be placed at three different distances from disk 2 (0.1, 0.35 and 1 m). Essentially, disks 1 and 2 control the wavelength resolution, whereas disk 3 in the standard configuration is mainly devoted to avoiding time overlap of the slowest neutrons of a given pulse with the fastest of the next one.

The collimator is basically made of two horizontal slits of half-widths r_1 and r_2 (numbered 1 and 2 with respect to the neutron direction) located between disks 2 and 3, at the same height and spaced apart by d_c = 1.8 m. The width of the slits can be tuned and chosen so that the angular resolution matches the wavelength resolution resulting from the disk chopper parameters: $\sigma_\theta/\theta \simeq \sigma_\lambda/\lambda$. In the following, we will consider three different typical configurations fulfilling this condition and corresponding to high (HR), medium (MR) and low resolution (LR), respectively (see Table 1).

Specular reflection at the desired angle θ_0 is obtained by rotation of the sample. In cases where a non-horizontal beam is needed (*e.g.* for the study of horizontal liquid surfaces), two plane mirrors are placed in the collimator to divert the beam. These mirrors have no impact on the resolution and will be ignored in the following. Specular reflection is measured in a vertical plane at an angle of $2\theta_0$ with a single detector whose area is wide enough to cross the trajectory of all reflected neutrons.

3. Wavelength resolution

The wavelength resolution essentially results from the incident beam distribution and the transfer function of the chopper. The latter is mainly controlled by the phases of the first two disks, but generally the third should also be accounted for at long wavelengths. In this section we examine these different points and present a way of calibrating the phases in question.

3.1. Basics of a double-disk chopper

We first consider a chopper made only of the first two disks. Let us denote x_k the positions (as in Table 1), $\varphi_{o,k} = \omega t_{o,k}$ the phase for disk opening and $\varphi_{c,k} = \omega t_{c,k}$ the phase for disk closure; see Table 2 for definitions of the principal variables used herein. By convention, we denote the actual phase as $\omega t - \varphi$, so that $\varphi > 0$ indicates a delay. The measurement consists of recording the number of neutron arrivals at the detector position x_d and time t_d over a timebase that is periodically restarted (triggered) at each revolution of the chopper. The accumulated record, obtained at time t_d, is referred to as a 'time-of-flight channel' (or t.o.f. channel) in the following. Fig. 2 shows the corresponding t.o.f. diagram using ωt as abscissa. From de Broglie's equation, in this diagram the kinematic curve of a neutron of wavelength λ and speed v is a straight line with the reciprocal slope

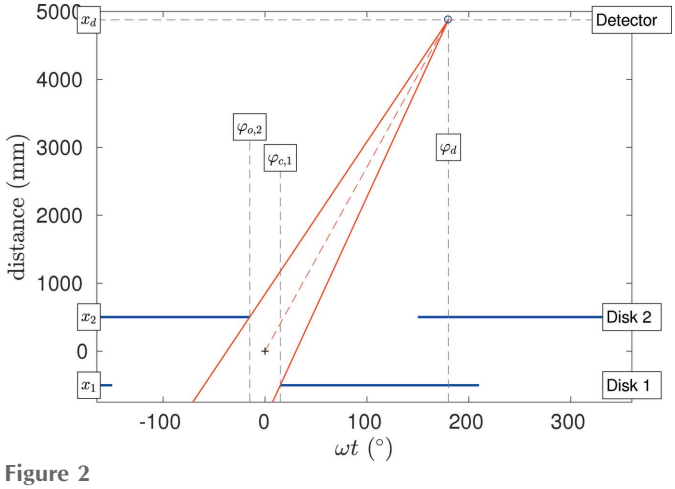

Figure 2
A double chopper: flight distance plotted versus phase ωt. Blue indicates the closed sectors of the disks. Neutrons that reach the detector at phase ωt_d have kinematics that lie between the two solid red lines, whose slopes are given by equation (2). Here $\omega\epsilon = -15°$, which is an exaggerated value chosen so that the drawing is clear.

Table 2
Table of symbols.

h_m	Ratio of Planck's constant to the mass of a neutron
g	Gravitational acceleration
v	Neutron speed
λ	Wavelength
ω	Chopper pulsation
t	Time
φ	$= \omega t$
δ	Tilt angle of the disk 1–disk 2 axis
η	Tilt angle of the disk 1–disk 3 axis
$t_{c,k}$, $t_{o,k}$	Closure and opening times for disk $k \in \{1, 2, 3\}$
t_d	Detection time (center of t.o.f. channel)
x_k	Position of disk $k \in \{1, 2, 3\}$
x_d, x_c, x_s	Positions of detector, middle of collimator and sample
x_{in}	Position of collimator entry
t_0	$= (t_{o,2} + t_{c,1})/2$
l	$= (x_2 - x_1)/2$
ϵ	$= (t_{o,2} - t_{c,1})/2$
L_i, L_j, L_k	$= x_d - x_i$ *etc.*
L	$= (L_1 + L_2)/2$
λ_1, λ_2	Wavelength boundaries of a given t.o.f. channel
λ_0	$= (\lambda_1 + \lambda_2)/2$, nominal wavelength
r_1, r_2	Half-widths of the first and second slits of the collimator
d_c	Distance between the two slits of the collimator
α_c	$= (r_1 - r_2)/d_c$, beam divergence due to collimation
r	Radius of disks
τ_p	Pulse half-width
τ_d	Half-width of t.o.f. channel
$\tau_{cr,c}$, $\tau_{cr,o}$	Crossing times for beam closure and opening
θ_0	Nominal specular reflection angle (tilt of the sample)
θ	Specular reflection angle
α	Deviation of neutrons due to beam divergence
γ	Deviation due to gravity at the sample position
$D(\lambda)$	Wavelength transmission probability density
$H_B(\lambda)$	Wavelength distribution of incident beam
$H(\lambda)$	Wavelength distribution on the sample
$P(\alpha)$	Angular distribution due to beam divergence
$J(\gamma)$	Angular distribution on the sample due to gravity
$G(\theta)$	Distribution of incidence angle
q	$= 4\pi \sin(\theta)/\lambda$, transfer vector magnitude
$R(q)$	Resolution function for transfer vector
$m(q)$	Theoretical reflectivity curve (model)
$M_{th}(q)$	Theoretical measurement of $m(q)$ accounting for $R(q)$
$M(q)$	Actual measurement of m

$$\frac{\omega}{v} = \frac{\omega}{h_m}\,\lambda, \tag{1}$$

where h_m is the ratio of Planck's constant to the mass of a neutron: $h_m \simeq 3956$ Å m s^{-1}.

Simple geometric considerations show that neutrons with a time of arrival t_d have a speed between v_1 and v_2, symbolized by the two solid red lines in Fig. 2, such that

$$\frac{1}{v_1} = \max\left\{0, \frac{t_d - t_{c,1}}{L_1}\right\} \quad \text{and} \quad \frac{1}{v_2} = \max\left\{0, \frac{t_d - t_{o,2}}{L_2}\right\}, \tag{2}$$

with $L_1 = x_d - x_1$ and $L_2 = x_d - x_2$. The wavelengths $\lambda_1 = h_m/v_1$ and $\lambda_2 = h_m/v_2$ correspond to these boundaries. Let us define

$$\begin{aligned} L &= (L_1 + L_2)/2, \\ t_0 &= (t_{o,2} + t_{c,1})/2, \\ l &= (x_2 - x_1)/2, \\ \epsilon &= (t_{o,2} - t_{c,1})/2. \end{aligned} \tag{3}$$

Note that ϵ can be either positive or negative ($\epsilon < 0$ in Fig. 2). Then the second terms in brackets in equation (2) can be rewritten as

$$\frac{1}{v_1} = \frac{(t_d - t_0) + \epsilon}{L_1} \quad \text{and} \quad \frac{1}{v_2} = \frac{(t_d - t_0) - \epsilon}{L_2}. \tag{4}$$

The half-range of the transmitted wavelength $\Delta\lambda$ and the median wavelength λ_0 are

$$\Delta\lambda = (\lambda_2 - \lambda_1)/2 \quad \text{and} \quad \lambda_0 = (\lambda_2 + \lambda_1)/2. \tag{5}$$

In the following, λ_0 will be referred to as the nominal wavelength of the t.o.f. channel at time t_d. One gets

$$\Delta\lambda = h_m \frac{l(t_d - t_0) - L\epsilon}{L_1 L_2} \quad \text{and} \quad \lambda_0 = h_m \frac{L(t_d - t_0) - l\epsilon}{L_1 L_2}. \tag{6}$$

In the case $\epsilon = 0$, one obtains

$$\Delta\lambda/\lambda_0 = l/L, \tag{7}$$

so that the relative resolution of the chopper is constant whatever the t.o.f. channel. This is the main reason for using a double-disk chopper as it allows us to optimize the resolution with respect to the neutron flux (van Well, 1992). From Table 1, the three standard configurations correspond to $\Delta\lambda/\lambda_0 = 1$, 4 and 10%, respectively. For comparison with other terms that play a role in the resolution, it is valuable to introduce a 'pulse half-width' $\omega\tau_p = \Delta\lambda\omega L/h_m$. For $\omega = 10^4{}^\circ\ s^{-1}$, $\epsilon = 0$, $L \simeq 4$ m and $2 < \lambda < 20$ Å, one has $0.2 < \omega\tau_p < 2^\circ$ at high resolution and $2 < \omega\tau_p < 20^\circ$ at low resolution.

3.2. Wavelength transmission function

For subsequent calculations of the exact resolution function, it is necessary to consider the probability density functions rather than the half-widths. The previous section can be formalized as follows. Let us consider the probability of a neutron of wavelength $\lambda = h_m/v$ reaching the detector at time t_d. The probability that this neutron passed through the first disk before it closed is the unit step function $f_1(\lambda) = [t_d - L_1/v < t_{c,1}] = [(t_d - t_{c,1})/L_1 < 1/v]$, where $[\ldots] = 1$ if the condition inside the brackets is true and 0 if not. The probability of passing the second disk after it opens is the unit step function $f_2(\lambda) = [t_{o,2} < t_d - L_2/v] = [1/v < (t_d - t_{o,2})/L_2]$. This can be rewritten as

$$\begin{aligned} f_1(\lambda) &= [\lambda_1 < \lambda], \\ f_2(\lambda) &= [\lambda < \lambda_2]. \end{aligned} \tag{8}$$

The probability density $D_0(\lambda)$ that a neutron of wavelength λ reaches the detector at time t_d is the probability of fulfilling these two independent conditions. Ignoring a normalization factor one gets

$$D_0(\lambda) = f_1(\lambda)\, f_2(\lambda) = [\lambda_1 < \lambda < \lambda_2]. \tag{9}$$

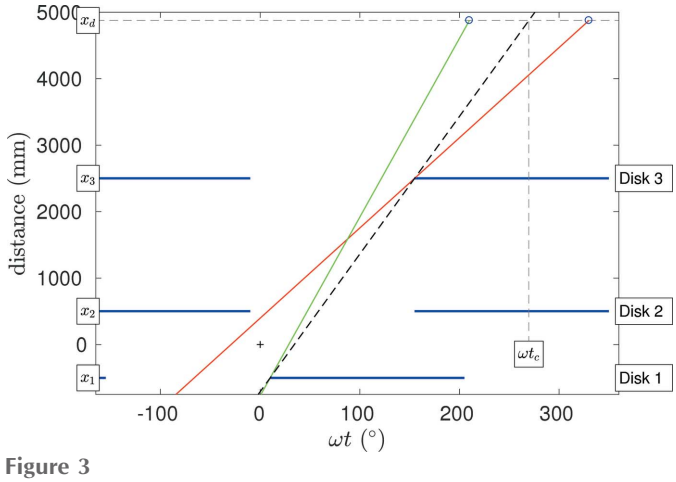

Figure 3
A three-disk chopper: in contrast to Fig. 2, the third disk comes into play for long times of flight. The dashed black line, with a slope $(x_3 - x_1)/(\varphi_{c,3} - \varphi_{c,1}) = (x_d - x_1)/(\omega t_c - \varphi_{c,1})$, delimits two regimes for the speed v_1 of the fastest neutrons of one given t.o.f. channel: v_1 is limited either by the closure of disk 1 (green) or by that of disk 3 (red). The same occurs for slow neutrons of speed v_2 (case not shown).

3.3. Three-disk chopper

The general case of a three-disk chopper is a little more complicated because the opening and closing in equation (9) that chops the neutron beam can come from any pair of disks. For instance, in Fig. 3, the speed v_1 of the fastest neutrons reaching the detector at time t_d is limited by the closure either of disk 1 (at a short time t_d) or of disk 3 (at a long time t_d). This can be formalized as follows. For each disk k let us denote

$$v_{c,k}^{-1} = \max\left\{0, \frac{t_d - t_{c,k}}{L_k}\right\} \quad \text{and} \quad v_{o,k}^{-1} = \max\left\{0, \frac{t_d - t_{o,k}}{L_k}\right\}. \tag{10}$$

Let us define the indices i, j such that

$$v_{c,i}^{-1} = \max_{k\in\{1,2,3\}}\left\{v_{c,k}^{-1}\right\} \quad \text{and} \quad v_{o,j}^{-1} = \min_{k\in\{1,2,3\}}\left\{v_{o,k}^{-1}\right\}. \tag{11}$$

All expressions of the previous section can then be generalized by replacing $(1, 2)$ by (i, j). Note that in a standard configuration $t_{c,1} \simeq t_{o,2} \simeq t_{o,3}$, so that the third disk comes into play only for long detection times. In this case, for most t.o.f. channels $(i, j) = (1, 2)$ this corresponds to the double-disk regime. However this is not general and (i, j), which depends on the relative phases of the three disks, also depends on the t.o.f. channel.

3.4. Crossing times and width of t.o.f. channel

The previous section implicitly considers a neutron beam of zero width. Because of its finite size, the beam opening (and closure) due to the passage of a disk is not instantaneous and not correctly described by a unit step function (Nelson, 2013). If the collimation is done with rectangular slits parallel to the edge of the disk windows, the transmitted beam area varies linearly with time, from 0 to its maximum value at a time $2\tau_{cr} = 2r_a/\omega r$, with r_a the half-width of the beam and r the radius of

the chopper disks. Actually, r_a depends on the beam divergence due to collimation (see Section 4.1) and thus on the position of the disk with respect to the collimator. Let us denote as r_1 and r_2 the half-widths of the two slits of the collimator, d_c their separation distance, and $\alpha_c = (r_1 - r_2)/d_c$. Then the half-width of the beam at a position x is

$$r_a(x) = r_1 + \alpha_c(x_{in} - x), \tag{12}$$

where x_{in} is the position of the collimator entry. For $x \simeq x_{in}$, $r_a(x) \simeq r_1$ (Nelson, 2013), but even if this condition is fulfilled for one disk of the pair (i, j), it may not be for the other because their positions are different. Thus, except in a case of particularly small beam divergence, the beam size is different for the two disks. Also, typical values for r_1, r_2 (Table 1) and $r =$ 300 mm give $\omega\tau_{cr}$ between 0.1 and 0.6°, which is not negligible compared with the pulse half-width $\omega\tau_p$ at short wavelength λ_0. The general expression for the beam size is then preferred. The corresponding crossing times for beam closure ($\tau_{cr,c}$) and opening ($\tau_{cr,o}$) are

$$\tau_{cr,c} = r_a(x_i)/\omega r \quad \text{and} \quad \tau_{cr,o} = r_a(x_j)/\omega r. \tag{13}$$

The unit step functions f_1 and f_2 for the probabilities of passing the first and second disks in equation (9) have to be replaced by two linear piecewise functions g_1 and g_2 corresponding to the linear variations of the corresponding beam areas between 0 and the maxima:

$$g_1(\lambda) = \begin{cases} 1 & t_d < t_c - \tau_{cr,c} \\ \frac{1}{2} + (t_c - t_d)/2\tau_{cr,c} & t_c - \tau_{cr,c} \le t_d \le t_c + \tau_{cr,c} \\ 0 & t_c + \tau_{cr,c} < t_d \end{cases}$$
$$g_2(\lambda) = \begin{cases} 0 & t_d < t_c - \tau_{cr,o} \\ \frac{1}{2} + (t_d - t_o)/2\tau_{cr,o} & t_o - \tau_{cr,o} \le t_d \le t_o + \tau_{cr,o} \\ 1 & t_o + \tau_{cr,o} < t_d \end{cases} \tag{14}$$

with $t_c = t_{c,i} + L_i/v$ and $t_o = t_{o,i} + L_j/v$. As a function of wavelength this can be rewritten in terms of convolution as

$$g_1(\lambda) = f_1(\lambda) * \left[-\frac{h_m\tau_{cr,c}}{L_i} < \lambda - \lambda_1 < \frac{h_m\tau_{cr,c}}{L_i} \right],$$
$$g_2(\lambda) = f_2(\lambda) * \left[-\frac{h_m\tau_{cr,o}}{L_j} < \lambda - \lambda_2 < \frac{h_m\tau_{cr,o}}{L_j} \right]. \tag{15}$$

The probability density for the transmission $g_1(\lambda)g_2(\lambda)$ is a piecewise function with up to five pieces [instead of a boxcar function for $D_0(\lambda)$] which is not symmetrical (because $\tau_{cr,c} \neq \tau_{cr,o}$ and $L_i \neq L_j$) and not always linear (*e.g.* for small $\lambda_2 - \lambda_1$).

Neutron counters record the number of neutron arrivals within the time interval $[t_d - \tau_d, t_d + \tau_d]$. For instance, 256 t.o.f. channels covering 360° of data acquisition give $\omega\tau_d \simeq 0.7°$, which is not always negligible compared with the pulse half-width $\omega\tau_p$, especially at short λ_0, and is comparable to the crossing times for beam closure and opening $\omega\tau_{cr,o}$ and $\omega\tau_{cr,c}$. In addition, note that, in order to gain increased counting statistics, channel binning is often performed after data acquisition. This operation amounts to use of a larger channel width τ_d. Similar to the crossing time, the effect of the channel width is not symmetrical for the disk i closure and disk j opening, because $L_i \neq L_j$. By taking into account the crossing times and channel widths, one can finally write the transmission function $D(\lambda)$ as

$$D(\lambda) = h_1(\lambda)h_2(\lambda), \tag{16}$$

with

$$h_1(\lambda) = g_1(\lambda) * \left[-\frac{h_m\tau_d}{L_i} < \lambda - \lambda_1 < \frac{h_m\tau_d}{L_i} \right], \tag{16a}$$

and

$$h_2(\lambda) = g_2(\lambda) * \left[-\frac{h_m\tau_d}{L_j} < \lambda - \lambda_2 < \frac{h_m\tau_d}{L_j} \right]. \tag{16b}$$

This again results in a piecewise function that would be a little tedious to write explicitly, because it consists of up to seven pieces with different cases to consider depending on the order of τ_p, τ_d, $\tau_{cr,c}$ and $\tau_{cr,o}$. Numerically, equation (16) can be computed as is (see Python module at https://bitbucket.org/LLBhermes/pytof/).

In Fig. 4, the ratio of the standard deviation σ of $D(\lambda)$ to its mean value $\overline{\lambda}$ is plotted for 256 t.o.f. channels covering 360° of a chopper revolution for the three typical configurations of Table 1. The curves show a plateau corresponding to the 'double-disk' chopper regime described by equation (7). At large $\omega\tau_d$ (large λ_0), the decrease in resolution is due to the third disk that comes into play, whereas at small $\omega\tau_d$ (small λ_0) departure from the plateau is due to the crossing times and the channel width.

The effect of channel binning on $D(\lambda)$ is plotted in Fig. 5 for the high-resolution configuration of Table 1. Basically, $D(\lambda)$ changes continuously from a nearly boxcar profile at large λ_0 to a 'bell curve' (but never Gaussian) at small λ_0. The t.o.f. channel at which this change appears is shifted to high λ_0 as the bin size increases.

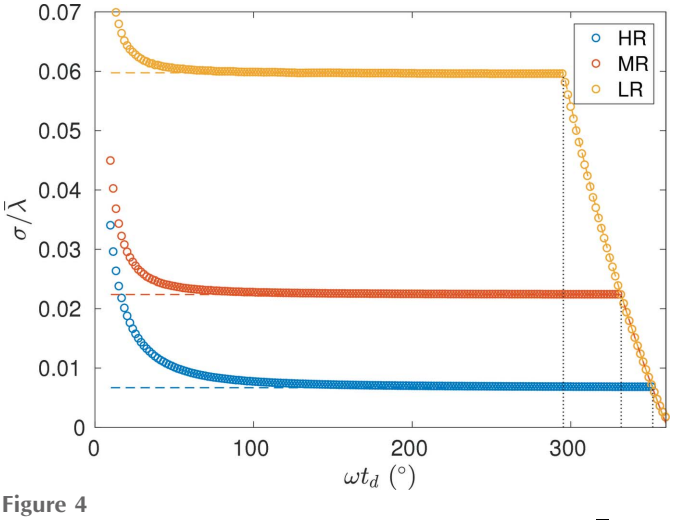

Figure 4
The ratio of the standard deviation σ of $D(\lambda)$ to the mean value $\overline{\lambda}$ versus the phase of t.o.f. channels for the three typical configurations described in Table 1. The dotted vertical lines mark the separation ωt_c of the two regimes delimited by the dashed line in Fig. 3.

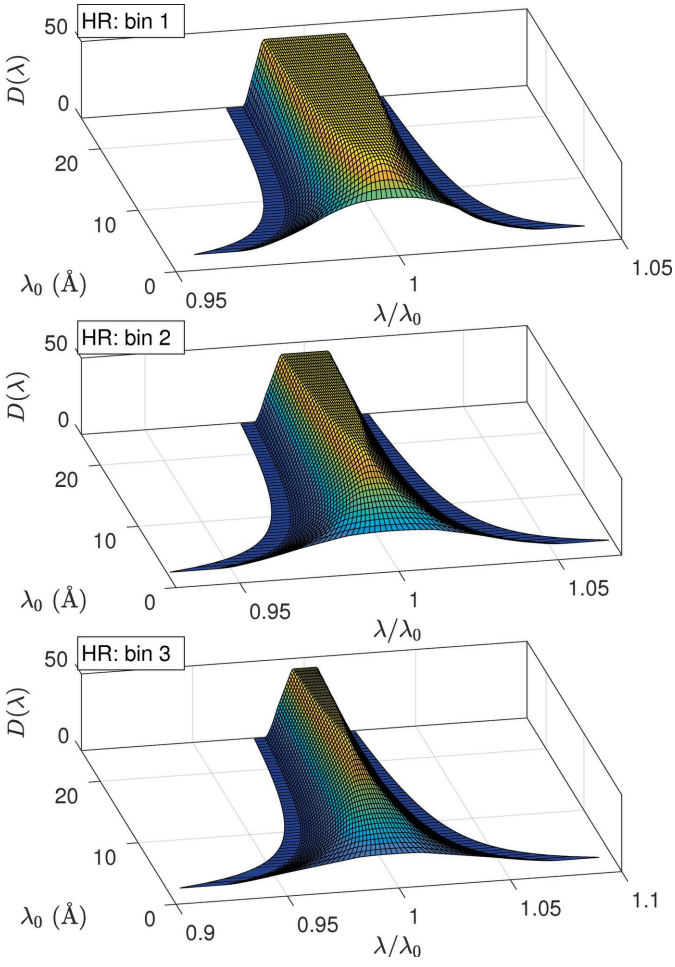

Figure 5
Wavelength distributions for the chopper transmission $D(\lambda)$ [equation (16)] versus λ/λ_0 (x axis) versus t.o.f. channel at a nominal wavelength λ_0 (y axis). Plots have been calculated for the high-resolution configuration (HR) of Table 1 with 300 (no channel binning), 150 (data binning by a factor 2) and 100 (data binning by a factor 3) t.o.f. channels from 30 to 300° of a chopper revolution.

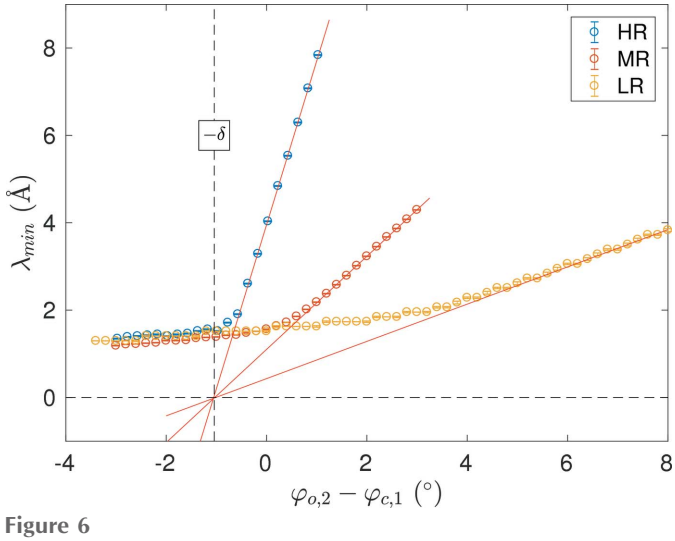

Figure 6
Minimum wavelength λ_{min} as a function of $\varphi_{o,2} - \varphi_{c,1}$, measured for the three different configurations of Table 1 at ω = 30 Hz. Extrapolation to $\lambda_{min} = 0$ gives the angle $\delta = (1 \pm 0.02)°$ that has to be added to the phase of disk 2.

3.5. Phase calibration and tilt of the chopper axis

Time-resolved neutron counting is triggered at each revolution by the chopper electronics. On this subject, the only unknown parameter is the phase shift φ_{trig} of this trigger with respect to the physical origin of phases. This point is resolved by measuring the transmission of a crystalline material (*e.g.* a graphite crystal) that displays a characteristic attenuation at a wavelength λ^* (Fermi *et al.*, 1947). No matter what the value of λ^*, the corresponding t.o.f. t^* is constant and the related phase is written as $\varphi^* = \omega t^* + \varphi_{trig}$. Measuring φ^* as a function of ω and extrapolating to $\omega = 0$ gives φ_{trig}.

Taking the rotation of disk 1 as reference, the phase shifts of disks 2 and 3 are chosen by the experimentalist and kept constant by the electronics with a control feedback loop, which ensures that no variation or drift occurs during measurements. However, possible differences between phase setpoints and their actual values have to be measured. Another point to consider is that a vertical tilt or misalignment of the centers of the three disks with the spectrometer axis affects the kinematic line of neutrons allowed to pass through the chopper in the same manner as a phase difference, hence the need for disk-phase calibration.

The phase of disk 2 affects the short-wavelength cut-off (λ_1) and the chopper resolution in the first regime of Fig. 4, whereas the phase of disk 3 affects the large-wavelength cutoff (λ_2) in the second regime and the t.o.f. channel at which this regime begins. Let us first consider the former. From Fig. 2, one can see that the fastest neutrons passing through the chopper are such that $\lambda_{min}/h_m = 1/v_{max} = \epsilon/l$. Measuring the transmission of the chopper, λ_{min} corresponds to the nominal wavelength of the t.o.f. channel at which the spectrum departs from the background. As the spectrum is quite abrupt in this region (see Fig. 8 in Section 3.7) this is very accurate. Of course, converting a channel to a wavelength assumes that we neglect the resolution function (because at this point we do not yet know it), but the consequence of this approximation is negligible as $\Delta\lambda$ is very small at short wavelengths. In Fig. 6,

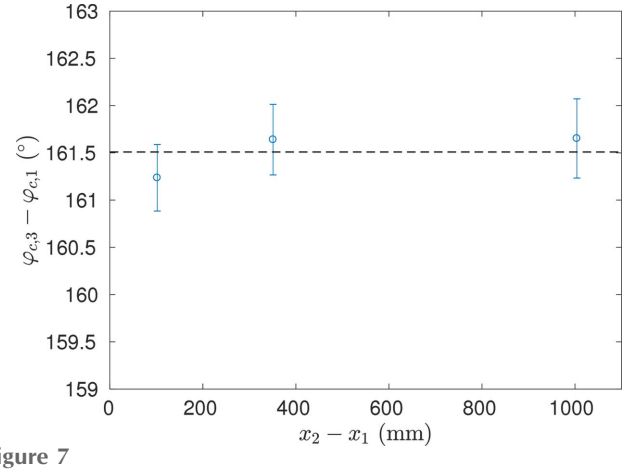

Figure 7
Value of the phase $\varphi_{c,3}$ deduced from equation (17) and the measurement of the phase ωt_c of the large-wavelength cut-off for a setpoint $\varphi_{c,3} = 165°$. The difference with this setpoint gives $\eta = -(3.5 \pm 0.3)°$, which has to be added to the phase of disk 3.

the measured $\lambda_{\min}$ is plotted as a function of $\varphi_{o,2} - \varphi_{c,1} = 2\omega\epsilon$. The linear behavior of the cut-off does not pass through the origin: a constant δ (here equal to 1° for the three configurations) should be added to $\varphi_{o,2} - \varphi_{c,1}$ in order to obtain the correct value for $\lambda_{\min}$. In practice, the phases $\varphi_{o,2}$ and $\varphi_{c,2}$ of disk 2 in all equations will be replaced by $\varphi_{o,2} + \delta$ and $\varphi_{c,2} + \delta$, and the corresponding times $t_{o,2}$ and $t_{c,2}$ changed accordingly. Note that this method for measuring $\varphi_{o,2}$ is equivalent to measuring the intensity of a monochromatic beam as a function of the phase $\varphi_{o,2} - \varphi_{c,1}$ (Gutfreund *et al.*, 2018), but is simpler to perform routinely because it does not require setting up a monochromator on the beamline.

In the same way, the large-wavelength cut-off of the chopper transmission allows us to determine the actual phase of disk 3. The phase ωt_c of the cut-off (see Fig. 3) is

$$\frac{\omega t_c - \varphi_{c,1}}{(x_d - x_1)/(x_3 - x_1)} = \varphi_{c,3}. \tag{17}$$

From the measurement of ωt_c the actual value of $\varphi_{c,3}$ can be deduced (Fig. 7). Here, we found that a constant value $\eta = -3.5°$ has to be added to the phase of disk 3. In the general case, the phases $\varphi_{o,3}$ and $\varphi_{c,3}$ of disk 3 in all equations will be replaced by $\varphi_{o,3} + \eta$ and $\varphi_{c,3} + \eta$, and the corresponding times $t_{o,3}$ and $t_{c,3}$ changed accordingly.

3.6. Effect of gravity on tilt angles

Because of gravity, a neutron's flight path is parabolic. The deviation from a straight line and a horizontal trajectory increases with the t.o.f., leading to actual values for the vertical tilt angles δ and η of the previous section that depend on wavelength.

Let us assume that the detector and the collimator slits are properly aligned with the neutron guide using a criterion of maximum neutron flux measured by integrating over the whole wavelength distribution. As neutrons of short wavelength are in the majority (see Fig. 8 in the next section) and neglecting their deviation due to gravity, the line joining the two slits of the collimator is almost horizontal. The apex of the parabolic trajectories of all neutrons is thus at the middle x_c between the two slits of the collimator. Let us denote $v_x = h_m/\lambda$ and v_z as the horizontal and vertical components of neutron velocity, respectively. At the apex, $v_z = 0$. At any other position x, the deflection angle ζ is $\tan^{-1}(v_z/v_x) \simeq v_z/v_x$. The t.o.f. to cover the distance $|x - x_c|$ is $|x - x_c|/v_x$, leading to $v_z = -g(x - x_c)/v_x$, with g the gravitational acceleration. Thus,

$$\zeta(x) = \frac{-g(x - x_c)}{v_x^2} = -(x - x_c)\frac{g}{h_m^2}\lambda^2, \tag{18}$$

with $g/h_m^2 \simeq 6.27 \times 10^{-7}$ m^{-1} Å^{-2}. Given two points (*e.g.* the edges of the two chopper disks i and j) on the parabola, the tangent at the middle is parallel to the chord. Thus, the tilt angles δ and η viewed by neutrons with parabolic trajectories are

$$\begin{aligned}\delta(\lambda) &= \delta(0) + \zeta\left(\frac{x_1 + x_2}{2}\right),\\ \eta(\lambda) &= \eta(0) + \zeta\left(\frac{x_1 + x_3}{2}\right).\end{aligned} \tag{19}$$

As these tilt angles have an effect on the boundaries λ_1 and λ_2 of each t.o.f. channel, gravity should affect the wavelength resolution. However, this effect is very small. For instance, in the double-disk regime $(i, j) = (1, 2)$, only δ is relevant and increases λ_2 by $h_m\zeta[(x_1 + x_2)/2]/\omega L_2$. For reflectometers a few metres long, $\zeta[(x_1 + x_2)/2]$ is around 0.01° and λ_2 is shifted by around 10^{-3} Å, which is clearly negligible.

3.7. Incident beam and detector efficiency

Thermal neutrons have a Maxwell–Boltzmann distribution of velocity that is altered by neutron guides. This distribution can not be measured directly, only its product $H_B(\lambda)$ with the detector efficiency which decays exponentially with wavelength. For a given t.o.f. channel, chopping a neutron beam amounts to applying the transmission $D(\lambda)$ of equation (16) to $H_B(\lambda)$ (Nelson, 2013) (see Fig. 8). The probability density of wavelengths for neutrons recorded in this channel is

$$H(\lambda) = H_B(\lambda)D(\lambda). \tag{20}$$

$H_B(\lambda)$ can be measured using a single-disk chopper with a small $\Delta\lambda$ (*i.e.* much smaller than the three-disk chopper) independent of the t.o.f. channel. For further calculations, $H_B(\lambda)$ can then be properly parametrized using an *ad hoc* function.

Note that measuring $H_B(\lambda)$ (which includes the detector efficiency) and using equation (20) gives us a way of accounting for the wavelength dependence of the detection time mentioned in the literature (Gutfreund *et al.*, 2018).

In Fig. 9, the wavelength distribution H is plotted for the different t.o.f. channels and for the three configurations of

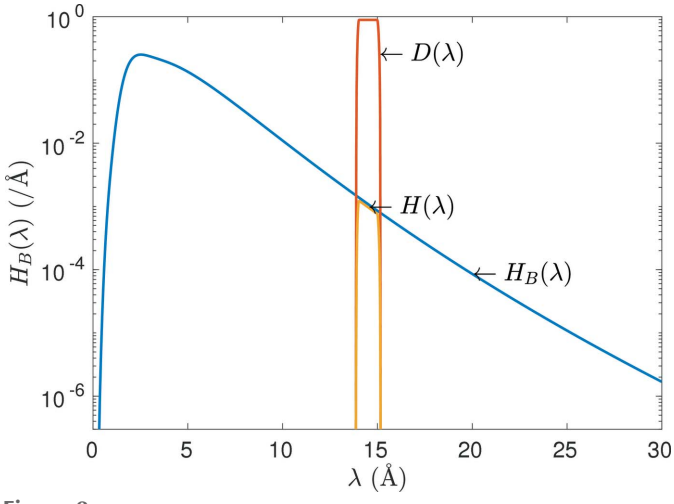

Figure 8
(Blue line) A plot of the effective wavelength distribution $H_B(\lambda)$ of the incident beam provided by the Orphée reactor on the neutron guide G6-2. (Red line) The transmission probability density $D(\lambda)$ for a t.o.f. channel at 180° computed for the low-resolution configuration of Table 1. (Orange line) The wavelength distribution $H(\lambda)$ (not normalized).

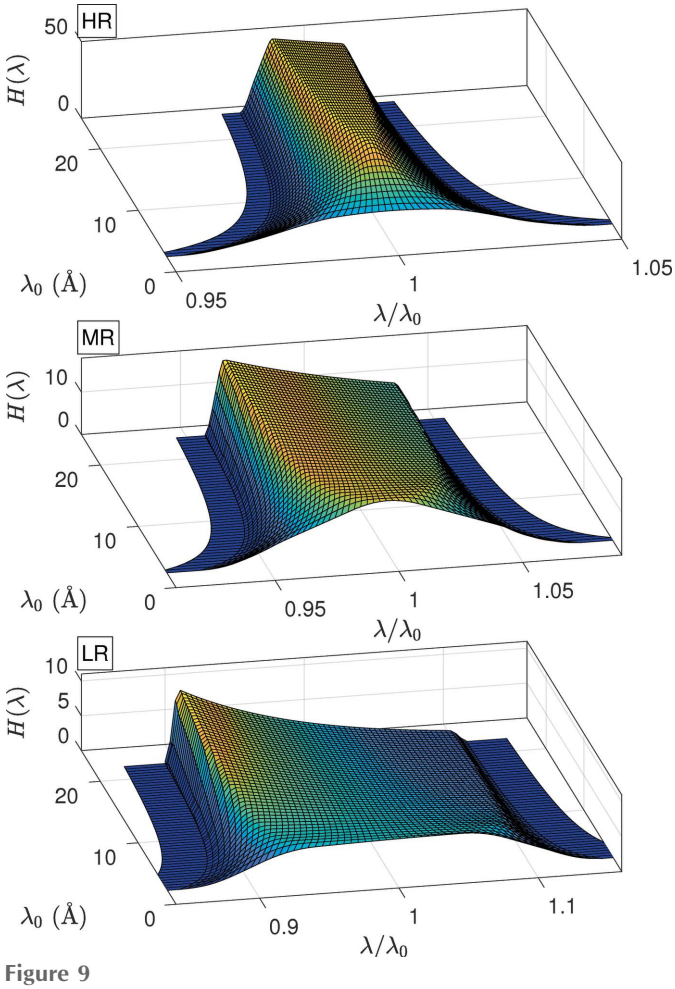

Figure 9
Wavelength distributions $H(\lambda)$ [equation (20)] versus λ/λ_0 (x axis) versus t.o.f. channel at a nominal wavelength λ_0 (y axis) for the three configurations of Table 1.

Table 1. The strong asymmetry of $H(\lambda)$ results in a mean wavelength $\overline{\lambda} = \int \lambda H(\lambda)\,\mathrm{d}\lambda$ significantly different from λ_0. In order to render this difference more clearly, we have plotted in Fig. 10 the ratio $\overline{\lambda}/\lambda_0$ as a function of the nominal wavelength λ_0 for the three different chopper configurations of Table 1. The wider the resolution, the more $\overline{\lambda}$ deviates from λ_0.

4. Angular resolution

In this section, we focus on beam collimation and gravity, which both contribute to the final distribution of neutron incidence angles on a sample.

4.1. Beam divergence

Let us consider the divergence in the vertical plane of a neutron beam collimated with two horizontal slits of half-widths r_1 and r_2, respectively, separated by a distance d_c. The distribution function $P(\alpha)$ of the angle of neutron trajectory results from the convolution of two boxcar functions centered on 0 and half-widths r_1/d_c and r_2/d_c, respectively:

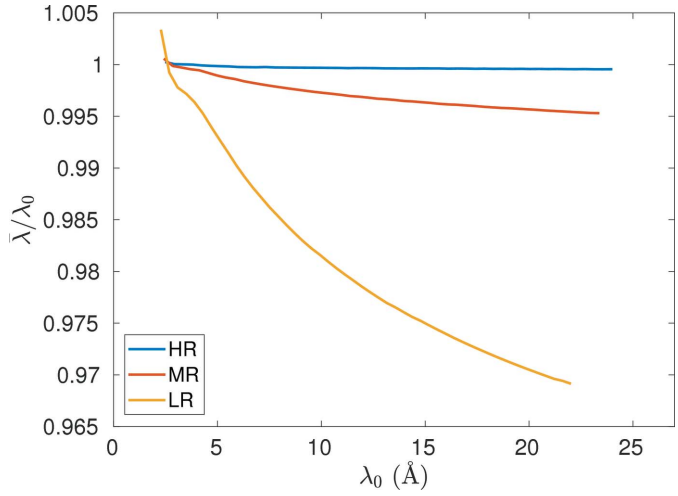

Figure 10
The ratios of the mean wavelength $\overline{\lambda}$ of the distribution $H(\lambda)$ to the nominal wavelength λ_0 versus λ_0 for the three configurations of Table 1.

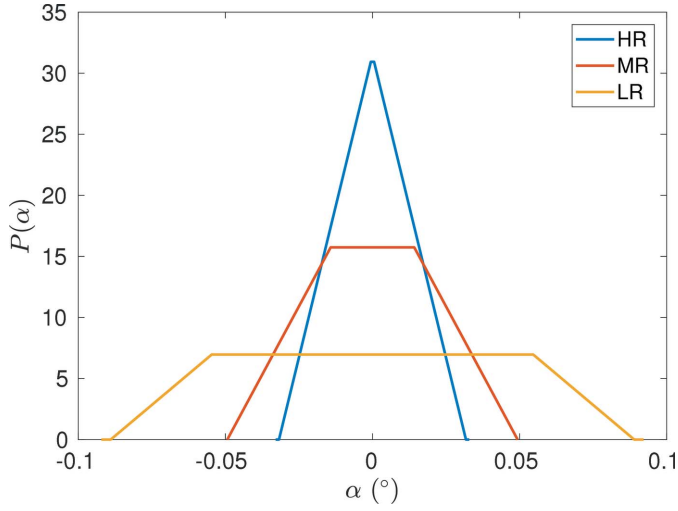

Figure 11
The typical angular distribution $P(\alpha)$ due to beam divergence for the three standard collimations of Table 1.

$$P(\alpha) = [-r_1/d_c < \alpha < r_1/d_c] * [-r_2/d_c < \alpha < r_2/d_c]. \quad (21)$$

This results in a symmetrical linear piecewise function. As convolution is commutative, the two boxcar functions are fully interchangeable, as also is the order of the values for r_1 and r_2 as far as only $P(\alpha)$ is concerned. However, for reasons related to the beam size [*e.g.* it is desired that the 'footprint' $2r_2\sin(\theta)$ be smaller than the sample size, and given that r_2 restrains the accuracy of the alignment of the sample], $r_1 > r_2$ is preferred and r_2 is kept constant. In Fig. 11 typical curves for $P(\alpha)$ are plotted for the standard collimations of Table 1.

The angular distribution $P(\alpha)$ so calculated implicitly assumes that the footprint of the beam on the sample (the part of the sample illuminated by the beam) is smaller than the size r_s of the sample in the x direction. In the case of a small sample and a very small tilt angle θ_0 of the sample with respect to the beam, it may be that this condition is not fulfilled: $2r_2 > r_s\sin(\theta_0)$. Then, $P(\alpha)$ has to be calculated only for the part of

the beam that reaches the sample. Equation (21) can account for this 'over-illumination' by replacing r_2 by $r_s \sin(\theta_0)/2$ and d_c by the distance between the first slit and the sample.

4.2. Deviation due to gravity

As mentioned in Section 3.6, gravity causes deviation of a neutron's trajectory. The angle of incidence of neutrons reaching the sample thus depends on their wavelength, which has to be accounted for if specular reflectivity is measured in the vertical plane (Bodnarchuk *et al.*, 2011).

If x_s is the position of the sample, from equation (18) the deviation angle (which is always negative) on the sample is

$$\gamma = \frac{-g(x_s - x_c)}{v_x^2} = -(c\lambda)^2 \quad \text{with} \quad c = \frac{[g(x_s - x_c)]^{1/2}}{h_m}. \quad (22)$$

The distribution $J(\gamma)$ of the deviation is related to the distribution of wavelengths $H(\lambda)$ via the general relation $J(\gamma) = H(\lambda)\,|\mathrm{d}\lambda/\mathrm{d}\gamma|$, with $\lambda = (-\gamma)^{1/2}/c$ [the inverse relation of equation (22)]. One obtains

$$J(\gamma) = \frac{1}{2c(-\gamma)^{1/2}}\, H\left[(-\gamma)^{1/2}/c\right]. \quad (23)$$

Basically, $J(\gamma)$ has a shape comparable to $H(\lambda)$. Let us denote as $[\gamma_1, \gamma_2]$ the support interval of $J(\gamma)$ and $\Delta\gamma = (\gamma_2 - \gamma_1)/2$. From equation (22), one obtains $\Delta\gamma = 2(c\lambda_0)^2\,(\Delta\lambda/\lambda_0)$. The quantity c is typically of the order of 8×10^{-4} Å^{-1} for $x_s - x_c =$ 1 m, and thus in a standard configuration $\Delta\gamma$ is small compared with the beam divergence [support of $P(\alpha)$]. However, if the relative angular resolution is very small compared with the wavelength resolution $H(\lambda)$, for instance in the case of t.o.f. channel binning to increase statistics (Cubitt *et al.*, 2015) or in the case of narrow collimation due to a small sample size *etc.*, then gravity should affect the width of the angular resolution. In any case, the main effect of gravity is due to the mean value $\overline{\gamma} = \int \gamma J(\gamma)\,\mathrm{d}\gamma$ which is nonzero and depends on the t.o.f. channel (*i.e.* on λ_0). In Fig. 12, the mean deviation $\overline{\gamma}$ is plotted as a function of λ_0.

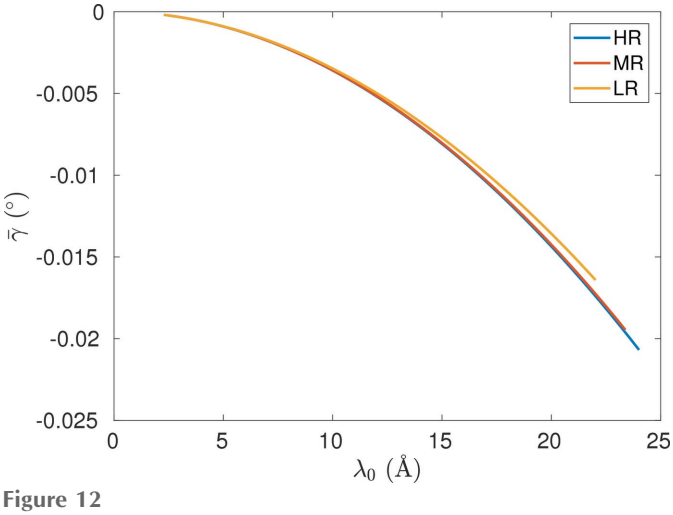

Figure 12
The mean deviation $\overline{\gamma}$ of neutrons due to gravity for $x_s - x_c = 1$ m versus λ_0 for the three configurations of Table 1.

Note that in the case of over-illumination of the sample (as discussed at the end of Section 4.1), the middle of the collimator has to be understood as being in between the first slit and the sample.

4.3. Distribution of incidence angle

Let us denote as θ_0 the nominal angle (*i.e.* the angle calculated from the inclination of the sample) of the neutron beam with respect to the interface under study. This angle is negative if neutrons come from below the interface and positive if they come from above it (this sign is imposed by gravity). The actual incidence angle θ of neutrons on the sample is

$$\theta = \theta_0 + \alpha - \gamma. \quad (24)$$

The distribution for θ is thus given by

$$G(\theta) = \int P(\theta - \theta_0 + \gamma)\, J(\gamma)\,\mathrm{d}\gamma. \quad (25)$$

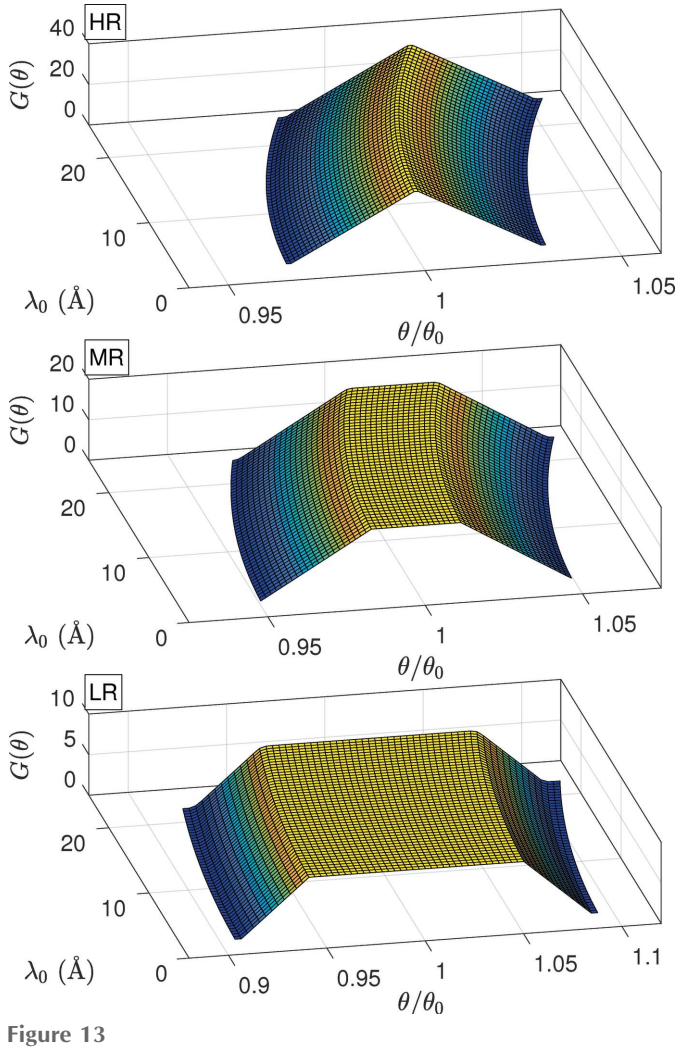

Figure 13
The angular resolution $G(\theta)$ versus θ/θ_0 (x axis, where $\theta_0 = 1°$ is the nominal angle) versus t.o.f. channel at a nominal wavelength λ_0 (y axis). Plots have been calculated for the three configurations of Table 1.

As $J(\gamma)$ is much narrower than $P(\alpha)$, its shape affects the shape of $G(\theta)$ only slightly but mainly induces an increase in the mean value $\overline{\theta}$ compared with the nominal value θ_0. Note that as γ is negative, and due to the sign in equation (24), gravity increases $|\theta|$ for $\theta_0 > 0$ but decreases $|\theta|$ for $\theta_0 < 0$. In Fig. 13, the angular resolution function $G(\theta)$ is plotted for $\theta_0 = 1^\circ$ for the different t.o.f. channels and the three typical configurations of the reflectometer.

Note that $G(\theta)$ is plotted here for didactic reasons but is not needed for the calculation of the overall resolution. Only its elementary components P and J are used in the next section.

5. Resolution of transfer vector

The physical parameter related to structural information on the measured samples is the magnitude of the transfer vector q (the conjugate variable of distance) which is defined as

$$q = 4\pi \sin(\theta)/\lambda. \tag{26}$$

However, the only directly adjustable parameters of the spectrometer are θ and λ, both being distributed around θ_0 and λ_0. For a given t.o.f. channel, the resolution function $R(q)$ of the transfer vector should thus be a generalized convolution of the probability densities $H(\lambda)$ (Fig. 9) and $G(\theta)$ (Fig. 13) whose corresponding random variables are combined following equation (26). However due to gravity, θ and λ are not strictly independent and convoluting their densities directly is not correct, even if it is a good approximation in standard configurations [because $J(\gamma)$ is narrow compared with $P(\alpha)$ in most cases]. Moreover, this approximation does not save computation time, so we prefer an exact treatment that will remain valid even when the width of J becomes significant (see Section 4.2).

For the sake of simplicity, let us first deal with the 'small-angle approximation' $\sin(\theta) \simeq \theta$. Then, using equation (24) the transfer vector magnitude is rewritten as

$$q = \frac{4\pi\theta}{\lambda} = 4\pi\frac{\theta_0 + \alpha - \gamma}{\lambda}, \tag{27}$$

where λ and α are random variables with densities $H(\lambda)$ and $P(\alpha)$, respectively, while $\gamma = -(c\lambda)^2$. Let us denote as $M(q)$ the measurement of the physical quantity $m(q)$. Quite generally, for one t.o.f. channel at $q_0 = 4\pi\theta_0/\lambda_0$ one can write

$$M(q_0) = \int \mathrm{d}\lambda\, H(\lambda) \int \mathrm{d}\alpha\, P(\alpha)\;\; m\left(4\pi\frac{\theta_0 + \alpha - \gamma}{\lambda}\right). \tag{28}$$

By using $\alpha = (\lambda q/4\pi) - \theta_0 - (c\lambda)^2$ and $\mathrm{d}\alpha = (\lambda/4\pi)\mathrm{d}q$, one can eliminate $J(\gamma)$ and obtain

$$\begin{aligned} M(q_0) &= \int \mathrm{d}\lambda\, H(\lambda) \int \mathrm{d}q\, \frac{\lambda}{4\pi}\, P\left[\frac{\lambda q}{4\pi} - \theta_0 - (c\lambda)^2\right] m(q) \\ &= \int \mathrm{d}q\, m(q) \int \mathrm{d}\lambda\, H(\lambda)\frac{\lambda}{4\pi}\, P\left[\frac{\lambda q}{4\pi} - \theta_0 - (c\lambda)^2\right]. \end{aligned} \tag{29}$$

By definition, the last integral is the resolution function of the transfer vector magnitude q:

$$R(q) = \int \mathrm{d}\lambda\, H(\lambda)\frac{\lambda}{4\pi}\, P\left[\frac{\lambda q}{4\pi} - \theta_0 - (c\lambda)^2\right]. \tag{30}$$

The same procedure can be used for the exact expression $q = 4\pi\sin(\theta_0 + \alpha - \gamma)/\lambda$, leading to $\alpha = \sin^{-1}(\lambda q/4\pi) - \theta_0 - (c\lambda)^2$ and $\mathrm{d}\alpha = \lambda \mathrm{d}q/[(4\pi)^2 - (\lambda q)^2]^{1/2}$. One obtains

$$R(q) = \int \mathrm{d}\lambda\, \frac{H(\lambda)\lambda P\left[\sin^{-1}(\lambda q/4\pi) - \theta_0 - (c\lambda)^2\right]}{4\pi\left[1 - (\lambda q/4\pi)^2\right]^{1/2}}. \tag{31}$$

Equation (31) can be numerically calculated as is (see Python module at https://bitbucket.org/LLBhermes/pytof/) from equations (16), (20) and (21). In Fig. 14, the whole resolution $R(q)$ is plotted for the three typical configurations as a function of t.o.f. channel for $\theta_0 = 1^\circ$. Firstly, notice the shift in the mean transfer vector value $\overline{q} = \int qR(q)\,\mathrm{d}q$ compared with q_0. This shift results from the wavelength distribution of the incident beam (Fig. 10) and from gravity (Fig. 12). Both effects contribute to the same result for $\theta_0 > 0$ but they oppose each other if $\theta_0 < 0$. To account for this effect properly, the simplest and most accurate way is to compute the exact resolution

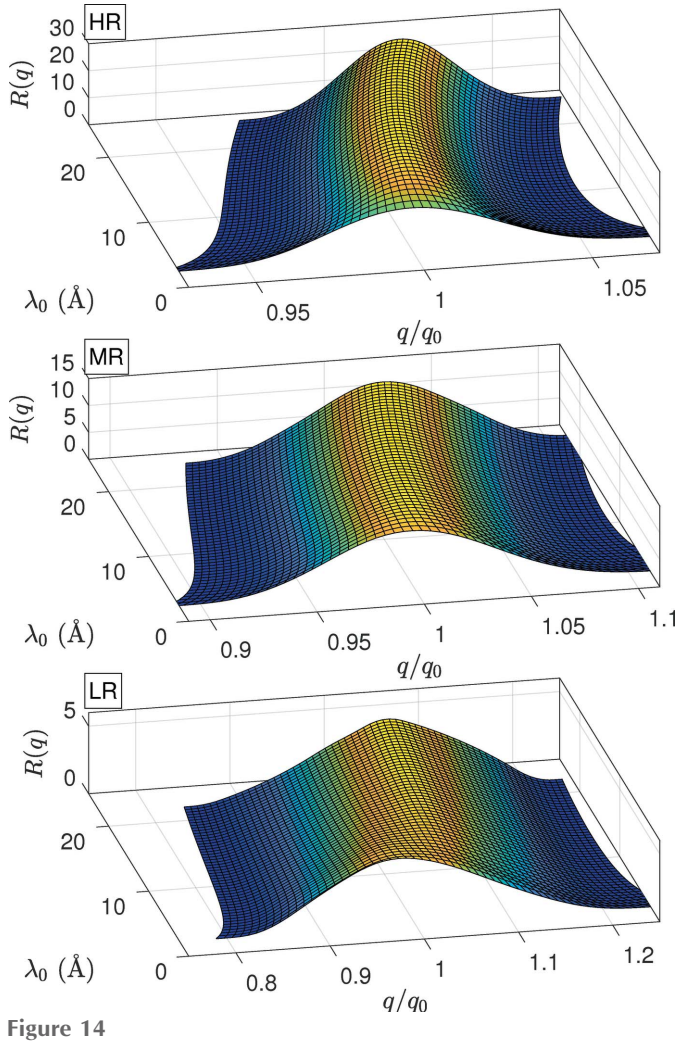

Figure 14
The total resolution $R(q)$ of the transfer vector magnitude q versus q/q_0 (x axis, where $q_0 = 4\pi\sin(\theta_0)/\lambda_0$ and $\theta_0 = 1^\circ$ is the nominal angle) versus t.o.f. channel at a nominal wavelength λ_0 (y axis). Plots have been calculated for the three configurations of Table 1.

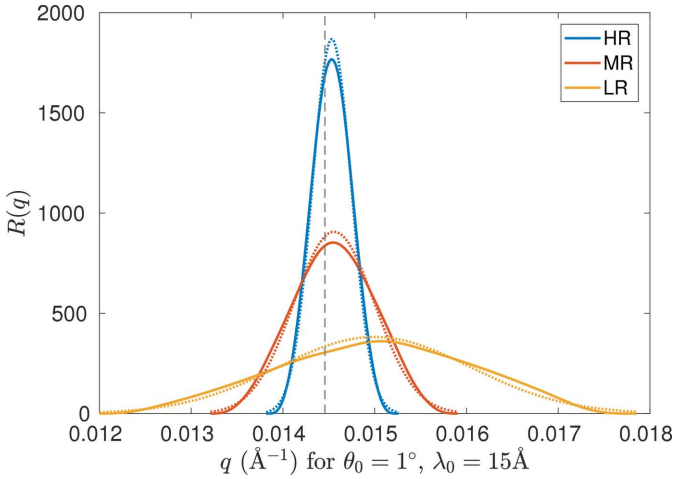

Figure 15
Plots of the exact resolution $R(q)$ (solid lines) versus transfer vector magnitude q for $\theta_0 = 1^\circ$ and $\lambda_0 = 15$ Å (cross sections of the 3D plots of Fig. 14) for the three configurations of Table 1. Dotted lines are Gaussian curves of the same mean and standard deviation.

function. Secondly, note that the profile of the exact resolution function differs from its Gaussian approximation (see Fig. 15). In any case, the exact resolution function has a compact support (*i.e.* R is nonzero inside a closed and bounded set of q values), unlike a Gaussian curve which should be cut numerically beyond an arbitrary multiple of the standard deviation. For the configuration allowing a wider resolution, the difference between the exact resolution and the Gaussian approximation is much more important and even the modal values differ. All these differences cannot reasonably be taken into account when summarizing the resolution with mean and standard deviation values.

6. Application

Let us consider the measurement M_k (performed with statistical error bars σ_k with $k \in \{1, 2, \ldots N\}$) of the reflectivity of a sample over N t.o.f. channels. We denote as $m(q, \mathbf{p})$ the theoretical reflectivity that depends on n physical parameters that make the coordinates of the vector $\mathbf{p}$. For a given t.o.f. channel k of resolution function R_k, the expected theoretical measurement $M_{\mathrm{th},k}$ is given by

$$M_{\mathrm{th},k}(\mathbf{p}) = \int m(q, \mathbf{p})\, R_k(q)\, \mathrm{d}q. \tag{32}$$

Let us define the mean relative distance χ^2 per channel between M and M_{th} as

$$\chi^2(\mathbf{p}) = \frac{1}{N} \sum_{k=1}^{N} \left[\frac{M_k - M_{\mathrm{th},k}(\mathbf{p})}{\sigma_k} \right]^2. \tag{33}$$

The parameter vector $\mathbf{p}$ can be determined experimentally by minimizing χ^2 following a standard numerical optimization procedure (curve fitting). The correctness of the resolution function can thus be evaluated (i) from the correctness of the parameter values thus determined and (ii) from the correctness of the final match between M and M_{th} [a low value for χ^2 and no correlation in the residual $(M - M_{\mathrm{th}})/\sigma$].

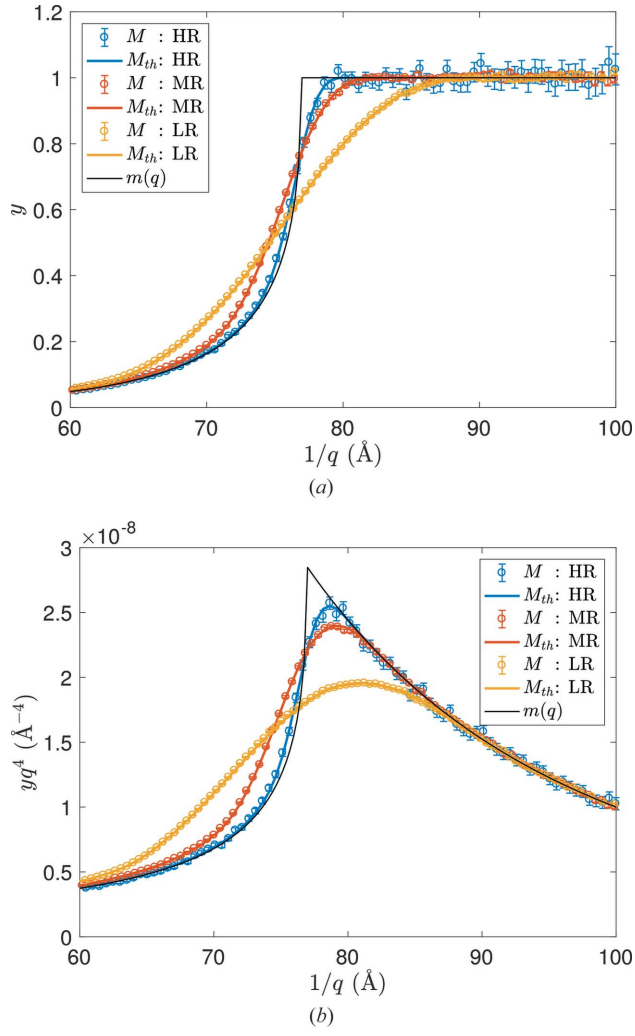

Figure 16
Reflectivity for an amorphous silica block in the region of the edge of total reflection. (Top) Measurement M, best fit M_{th} [equation (32)] and model $m(q)$ [equation (34)] versus $1/q$ (because the channels are almost regularly spaced in wavelength). (Bottom) The same data with the y coordinates multiplied by q^4. For these best fits, $q_c = 1.298$, 1.306 and 1.292×10^{-2} Å^{-1} and $\chi^2 = 1.11$, 3.97 and 3.51 for the high-resolution, medium-resolution and low-resolution configurations, respectively.

For such an evaluation, the sample candidate should display a strong variation in reflectivity in the accessible q range, in order to maximize the effect of convolution by the resolution function [equation (32)] with a minimum number of unknown parameters (coordinates of $\mathbf{p}$). From this point of view, the reflectivity near the total reflection plateau of the interface between air and a smooth and pure solid is probably the most suitable. We have chosen an amorphous silica block with a polished surface, for which the reflectivity can be written

$$m(q) = \left[\frac{q - (q^2 - q_c^2)^{1/2}}{q + (q^2 - q_c^2)^{1/2}} \right]^2 \exp\left[-\sigma_h^2 q \left(q^2 - q_c^2 \right)^{1/2} \right]. \tag{34}$$

The first term of this product is the Fresnel reflectivity of a perfectly flat surface, where $q_c = (16\pi\rho)^{1/2}$ is the edge of the total reflectivity plateau and ρ the scattering length density of amorphous silica. The second term accounts for the surface roughness of characteristic height σ_h. Measurements were done in the three configurations of Table 1 for $\theta_0 = 1^\circ$. The results and data fitting are plotted in Fig. 16. For the three configurations, the values for χ^2 at the optimum are very small, and the values determined for q_c are in very good agreement and consistent with the density of amorphous silica [here, $\overline{q}_c = (1.300 \pm 0.006) \times 10^{-2}$ Å^{-1} leads to (2.13 ± 0.02) g cm^{-3} for the density of amorphous silica]. Note that the increase in χ^2 with the broadening of the resolution is simply due to the gain in flux resulting in smaller statistical error bars σ_k in equation (33).

The use of the exact resolution function as plotted in Fig. 14 could appear unnecessarily tricky compared with the use of a Gaussian curve of the same average and standard deviation. This is not the case for two reasons. First, the calculation of the exact resolution function is needed anyway to determine the average and standard deviation values of the Gaussian approximation curve, and secondly, once this is achieved, convolution by the exact resolution or its Gaussian approximation requires the same computing power. Also, convolution by the exact resolution function will always produce better results, in particular at low resolution. Best fits obtained using the Gaussian approximation (computed over a support half-width equal to three times the standard deviation) of the exact resolution function were done for the examples given in Fig. 16. The corresponding χ^2 values are 1.54, 15.1 and 218 (instead of $\chi^2 = 1.11$, 3.97 and 3.51 with the exact function) for the HR, MR and LR configurations, respectively. In Fig. 17 (top) the results for the two fits are compared for the LR configuration of Table 1. The differences are subtle but they are emphasized by plotting the residual $(M - M_{th})/\sigma$ (Fig. 17, bottom) which clearly shows correlations in the case of the Gaussian approximation. It is important to emphasize that the Gaussian approximation that we are discussing here should not be confused with the resolution function that would be calculated following the central-limit theorem, *i.e.* by adding the variances of each term. Here, as the mean and standard deviation values are correctly calculated (from the exact resolution function), fitting using one or the other resolution curve does not lead to significant differences in the parameter best values, or in their confidence intervals, although the χ^2 values are very different. However, the Gaussian resolution curve that could be produced by applying the central-limit theorem leads to much less satisfactory parameter values. The computation of the exact resolution profile is thus mandatory to reach the most accurate data-fitting results.

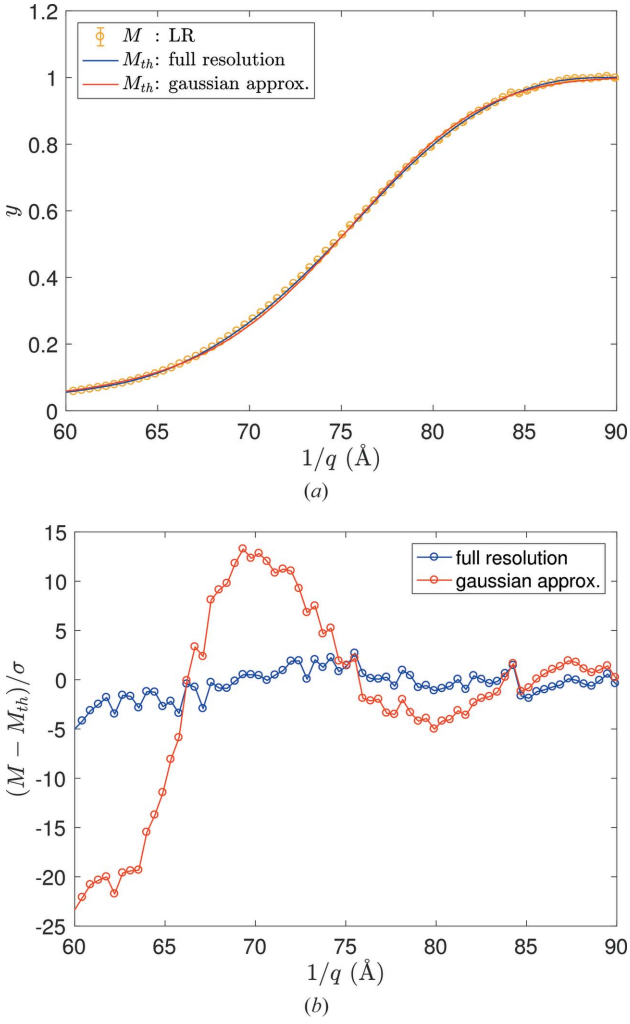

Figure 17
Reflectivity for an amorphous silica block in the region of the edge of the total reflection plateau. (Top) Measurement M and best fits M_{th} using the exact resolution or its Gaussian approximation (computed over an interval half-width equal to three times the standard deviation). (Bottom) $(M - M_{th})/\sigma$. The use of the exact resolution leads to $\chi^2 = 3.51$ and of its Gaussian approximation to $\chi^2 = 218$.

By definition, using the exact resolution function is more accurate than using its Gaussian approximation, but it also saves time. Computation of the exact resolution function is done only once during data reduction. The time spent is negligible compared with the time needed for data fitting, which consists of many iterations of the convolution of a theoretical model by the resolution. The exact resolution function has a compact support, whereas its Gaussian approximation does not. Thus for a given high percentile, the Gaussian approximation needs a more extended sampling and thus is more time consuming during the data-fitting stage than the exact function. This removes a lot of interest in the approximation.

7. Conclusions

In this paper we have presented the calculation of the exact and comprehensive resolution function for a t.o.f. neutron reflectometer in a way that accounts for all contributions without any assumption of the Gaussian distribution or independence of the corresponding variables. The step-by-step procedure comes with a fully documented Python module (https://bitbucket.org/LLBhermes/pytof/), whose routines

match the equations and terminology of this paper. The module can be easily used for numerical applications to any specific case, from the computation of the resolution to data fitting. In addition, the module allows the reader to reproduce most of the figures of this paper and to change their parameters easily.

We have shown that, if the resolution is relaxed, the resulting resolution function departs strongly from a Gaussian profile and using the exact function provides much more accurate results. This point will be highly relevant with the emergence of compact and low-flux neutron sources (see *e.g.* Ott, 2018) which will probably require such relaxed resolutions.

Here we have tried to treat the different contributions to the resolution of a t.o.f. neutron reflectometer in an exhaustive but still general manner. However, some peculiar points, which would require special attention, have not been examined, mainly detector resolution and pixel binning (Cubitt *et al.*, 2015) if a position-sensitive detector is used, and non-flat samples (Cubitt *et al.*, 2015). We hope this paper will help to manage these particular cases.

References

Bodnarchuk, I., Manoshin, S., Yaradaikin, S., Kazimirov, V. & Bodnarchuk, V. (2011). *Nucl. Instrum. Methods Phys. Res. A*, **631**, 121–124.

Cousin, F. & Chennevière, A. (2018). *EPJ Web Conf.* **188**, 04001.

Cubitt, R., Saerbeck, T., Campbell, R. A., Barker, R. & Gutfreund, P. (2015). *J. Appl. Cryst.* **48**, 2006–2011.

Fermi, E., Sturm, W. J. & Sachs, R. G. (1947). *Phys. Rev.* **71**, 589–594.

Gutfreund, P., Saerbeck, T., Gonzalez, M. A., Pellegrini, E., Laver, M., Dewhurst, C. & Cubitt, R. (2018). *J. Appl. Cryst.* **51**, 606–615.

Nelson, A. R. J. & Dewhurst, C. D. (2013). *J. Appl. Cryst.* **46**, 1338–1346.

Ott, F. (2018). *Compact Neutron Sources for Neutron Scattering*. Technical Report. CEA Paris Saclay, France. https://hal-cea.archives-ouvertes.fr/cea-01873010.

Well, A. A. van (1992). *Physica B*, **180–181**, 959–961.

Well, A. A. van & Fredrikze, H. (2005). *Physica B*, **357**, 204–207.